REPORT

Evidence for field induced quantum spin liquid behavior in a spin-1/2 honeycomb magnet

Gaoting Lin,[1,11] Mingfang Shu,[1,10,11] Qirong Zhao,[2,11] Gang Li,[3] Yinina Ma,[3] Jinlong Jiao,[1] Yuting Li,[1] Guijing Duan,[2] Qing Huang,[4] Jieming Sheng,[5] Alexander I. Kolesnikov,[6] Lu Li,[7] Liusuo Wu,[5] Hongwei Chen,[8] Rong Yu,[2,9] Xiaoqun Wang,[1] Zhengxin Liu,[2,9,*] Haidong Zhou,[4,*] and Jie Ma[1,9,*]

*Correspondence: liuzxphys@ruc.edu.cn (Z.L.); hzhou10@utk.edu (H.Z); jma3@sjtu.edu.cn (J.M.)

Received: March 8, 2024; Accepted: June 26, 2024; Published Online: July 2, 2024; https://doi.org/10.59717/j.xinn-mater.2024.100082

GRAPHICAL ABSTRACT

PUBLIC SUMMARY

- Field-induced quantum spin liquid state in spin-1/2 honeycomb magnet $Na_2Co_2TeO_6$ is highly desired.
- The absence of symmetry breaking is realized by the persistence of C_6 symmetry under a magnetic field.
- The continuum and Variational Monte Carlo simulation support the field-induced quantum spin liquid state.

REPORT

Evidence for field induced quantum spin liquid behavior in a spin-1/2 honeycomb magnet

Gaoting Lin,[1,11] Mingfang Shu,[1,10,11] Qirong Zhao,[2,11] Gang Li,[3] Yinina Ma,[3] Jinlong Jiao,[1] Yuting Li,[1] Guijing Duan,[2] Qing Huang,[4] Jieming Sheng,[5] Alexander I. Kolesnikov,[6] Lu Li,[7] Liusuo Wu,[5] Hongwei Chen,[8] Rong Yu,[2,9] Xiaoqun Wang,[1] Zhengxin Liu,[2,9,*] Haidong Zhou,[4,*] and Jie Ma[1,9,*]

[1]Key Laboratory of Artificial Structures and Quantum Control, School of Physics and Astronomy, Shanghai Jiao Tong University, Shanghai 200240, China

[2]Department of Physics, Renmin University of China, Beijing 100872, China

[3]Beijing National Laboratory for Condensed Matter Physics, Institute of Physics, Chinese Academy of Sciences, Beijing 100190, China

[4]Department of Physics and Astronomy, University of Tennessee, Knoxville 37996, USA

[5]Shenzhen Institute for Quantum Science and Engineering (SIQSE) and Department of Physics, Southern University of Science and Technology, Shenzhen 518055, China

[6]Neutron Scattering Division, Oak Ridge National Laboratory, Oak Ridge 37831, USA

[7]Department of Physics, University of Michigan, Ann Arbor 48109, USA

[8]College of Materials Science and Chemistry, China Jiliang University, Hangzhou 310018, China

[9]Collaborative Innovation Center of Advanced Microstructures, Nanjing University, Nanjing 210093, China

[10]Guangdong Provincial Key Laboratory of Extreme Conditions, Dongguan 523803, China

[11]These authors contributed equally

*Correspondence: liuzxphys@ruc.edu.cn (Z.L.); hzhou10@utk.edu (H.Z); jma3@sjtu.edu.cn (J.M.)

Received: March 8, 2024; Accepted: June 26, 2024; Published Online: July 2, 2024; https://doi.org/10.59717/j.xinn-mater.2024.100082

Citation: Lin G., Shu M., Zhao Q., et al., (2024). Evidence for field induced quantum spin liquid behavior in a spin-1/2 honeycomb magnet. The Innovation Materials **2(3)**: 100082.

One of the most important issues in modern condensed matter physics is the realization of fractionalized excitations, such as the Majorana excitations in the Kitaev quantum spin liquid. To this aim, the 3*d*-based Kitaev material $Na_2Co_2TeO_6$ is a promising candidate whose magnetic phase diagram of **B** // **a*** contains a field-induced intermediate magnetically disordered phase within 7.5 T < |B| < 10 T. The experimental observations, including the restoration of the crystalline point group symmetry in the angle-dependent torque and the coexisting magnon excitations and spinon-continuum in the inelastic neutron scattering spectrum, provide strong evidence that this disordered phase is a field induced quantum spin liquid with partially polarized spins. Our variational Monte Carlo simulation with the effective K-J_1-Γ-Γ'-J_3 model reproduces the experimental data and further supports this conclusion.

INTRODUCTION

Quantum spin liquids (QSLs) are exotic phases of matter resulting from competing interactions or geometric frustration. Due to the long-range quantum entanglement in the QSL ground states, interesting phenomena can arise, such as the collective excitations with fractional quantum numbers and the emergence of gauge fluctuations.[1,2] A lot of efforts have been made to search for QSL phase with Heisenberg-type exchange interactions in geometrically-frustrated systems, including the triangular lattice, kagomé lattice, and three-dimensional structures such as the hyper-kagomé lattices.[2-8] Meanwhile, anisotropic interactions resultant from spin-orbital coupling (SOC) have attracted more and more interests.[1,9-33] A paradigmatic example is the exactly solvable Kitaev model on the honeycomb lattice which hosts QSL ground state and Majorana-fermion-like elementary excitations.[8]

Recently, exciting progress has been made on the Kitaev spin liquid candidates from the 3*d*/4*d*/5*d* transition metal Co/Ru/Ir for the low-energy effective interactions, which contain the Kitaev-type exchange terms due to the peculiar lattice structure and the SOC.[1,15-31,34-38] However, owing to the existence of non-Kitaev interactions, all of these materials exhibit zigzag antiferromagnetic (AFM) order at low temperatures. Besides the Heisenberg exchanges, the off-diagonal symmetric interactions of the Γ and Γ' terms were proposed to construct their low-energy effective model.[16-19,23,24,36] Unlike the Ru- and Ir- materials,[19,36,38] the 3*d* orbitals in the Co-based materials are more compact and the contributions from the SOC channels t_{2g}-e_g and e_g-e_g can weaken the Γ and Γ' exchanges.[24,38]

One of the most representative Kitaev materials among the 3*d*-cobalt magnets is the $Na_2Co_2TeO_6$ (NCTO),[1,24,29,34,35,39-44] in which the honeycomb layers are formed by the magnetic Co^{2+} ions surrounded by the O^{2-} octahedrons (Figures 1A-B). The principal reciprocal vectors **a*** (crystallographic vector **a**) direction is parallel (perpendicular) to the Co-Co bond, which corresponds to the [$\bar{1}$10] ([$\bar{1}2\bar{1}$]) direction in the spin coordinate (Supplementary Figure S1). NCTO presents a zigzag AFM order below $T_N \approx 26$ K and another two anomalies at $T_F \approx 15$ K and $T* \approx 7$ K (Figures S2A-B).[1,35,41-44] The zigzag order in NCTO can be easily suppressed by a magnetic field parallel to the **a***-axis, leading to an intermediate field-induced magnetically disordered phase above ~ 7.5 T before entering a trivial polarized phase near 10 T.[1,44] The exact nature of this intermediate phase, most intriguingly, whether it belongs to a QSL, is still illusive and deserves further investigation.[1]

The study of zero-field spin-wave excitations of NCTO indicates that while the AFM third-neighbor Heisenberg exchange interaction J_3 is fairly large,[1,29,34] the Kitaev term cannot be ignored.[24,29] Several theoretical works have estimated the value of *K*, however, it varies from large to small, even its sign from ferromagnetic to AFM.[1,24,29,34,35,38,41,45,46] It is reasonable to expect that the SOC caused bond-dependent interactions, including the Kitaev term, play an important role in understanding the rich phase diagram of NCTO in magnetic fields (Figure 1C).

In the present work, we studied the nature of the field-induced intermediate magnetically disordered phase of a single-crystal NCTO via magnetic torque and inelastic neutron scattering (INS) spectroscopy. Under low temperatures and low fields, the torque is very weak and exhibits a 2-fold (C_2) symmetric angular dependence, which confirms the AFM long-range order. The AFM order vanishes above 7.5 T as the lattice 6-fold (C_6) symmetry is restored in the angular dependence of the torque, which is verified by the disappearance of Bragg peaks at the M-point at B = 8 T (Figures 1D-E). The material enters the polarized phase at 10 T where a phase transition is observed in the differential magnetic susceptibility as well as the differential torque (Figure 1G). The region between 7.5 T and 10 T is shown to be a field-induced QSL phase with partial spin polarization and strong quantum fluctuations. With an 8 T magnetic field along the **a*** direction, the intensity of INS spectra at the M-point is suppressed, while gapped spin-wave bands show up at 1.5 meV~2.5 meV and 3 meV~4 meV in the vicinity of the Γ-point (resulting from the partial polarization of the spins) and an intense 'Λ' shape spinon continuum appears at 4 meV~8 meV. These features are consistent with a theoretically computed dynamical structure factor of a field-induced partially polarized QSL phase.

MATERIALS AND METHODS

Sample preparation and characterization

The high-quality single crystals were grown by the flux method. The polycrystalline sample of NCTO was mixed with the flux of Na_2O and TeO_2 in molar ratio of 1:0.5:2 and gradually heated to 900°C at 3 °C/min in air after grinding. The sample was retained at 900°C for 30 h, and was cooled to a temperature of 500°C at the rate of 3 °C/h. The furnace was then shut down.[1]

Magnetization and heat capacity

The magnetization measurements were performed by using a vibrating

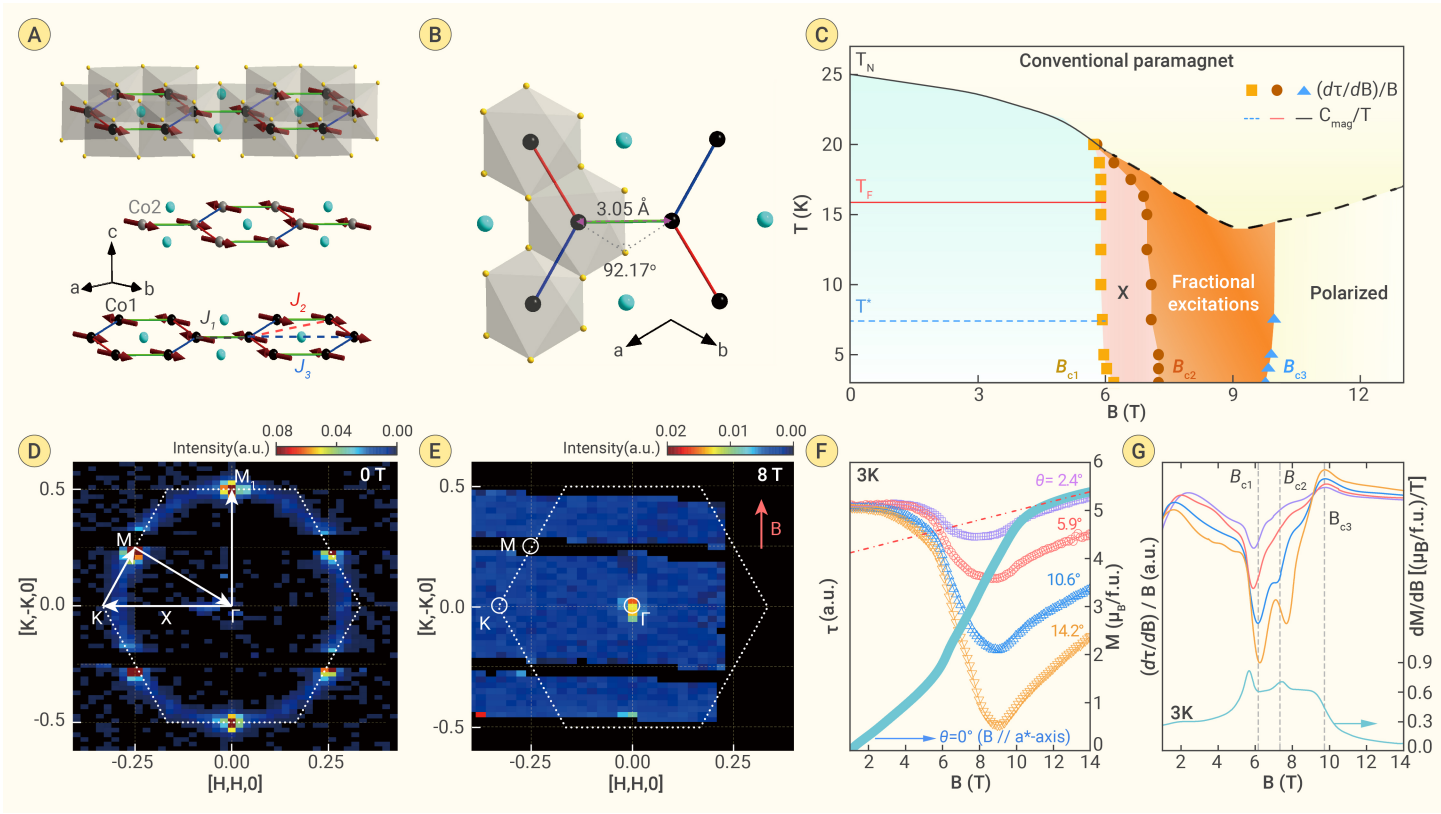

Figure 1. Structure, magnetic properties and temperature-field phase diagram of NCTO (A) Three-dimensional stacking of the Co honeycomb layers. Honeycomb network shows the Co-Co bonds (red/blue/green) and edge-shared CoO_6 octahedra (the black, grey, cyan and golden spheres represent Co1, Co2, Te and O atoms, respectively). The Co1 and Co2 honeycomb layers present the ABAB-type layer stacking along the *c* axis. The dark red refers to the direction of moments that are in the *ab* plane and parallel to *b*-axis, indicating a zigzag AFM ground state.[42,43] (B) A honeycomb network with three selected adjacent edge-shared CoO_6 octahedra. In the $P6_322$ structure, Co ions form a perfect honeycomb lattice with an equal 92.17° Co-O-Co bond angle and the nearest-neighbor Co-Co bond length $d_{Co\text{-}Co}$ = 3.05 Å. (C) Temperature-field phase diagram with B parallel to Co-Co bonds. The phase boundaries are deduced from the temperature-dependent magnetic specific heat C_{mag}/T with B // a* (Supplementary Figure S2E) and field-dependent differential magnetic torque $\frac{1}{B}\frac{d\tau}{dB}$ with 10.6° away from a* (Supplementary Figure S7). When the AFM order is suppressed by field, the sharp discontinuity in C_{mag}/T at T_N labeled by the black solid line becomes crossover type wide peaks presented by the dashed dark line. The critical fields B_{C1}, B_{C2}, and B_{C3} are determined by the $\frac{1}{B}\frac{d\tau}{dB}$ curves at 10.6 degree. Elastic neutron scattering results integrated over L = [-2.5, 2.5] and E = 0 = ± 0.05 meV at 0 T (D) and 8 T (E). The white dashed lines represent the Brillouin zone boundaries. The high symmetry points Γ, X, K, M and M_1 are marked in (D). The red arrow in (E) shows the applied magnetic field B // a*-axis. (F) Field dependence of magnetic torque of NCTO measured at 3 K with field along selected angles. The solid lines are the polynomial fitting of magnetic torque ratio. (G) The detivative $\frac{1}{B}\frac{d\tau}{dB}$ curves are calculated from the fitted data. θ is the angle between B and the a* and with respect to the real-space orientation of the Co-Co bonds. More details see the supplementary Figure S1. For better comparison, the field dependence of magnetization M(B) (F) and the derivative dM(B)/dB (G) are also shown with B // a*. The red dashed line shows the Van-Vleck paramagnetic background, which suggests that the saturation field is around B_S =12.5 T and the saturation magnetization is about $M_S = 2.05\mu_B/Co^{2+}$.

sample magnetometer (VSM) in the physical properties measurement system (PPMS Dynacool-9 system, Quantum Design) with field up to 9 T. The heat capacity measurements were carried out using the relaxation method in another PPMS with field up to 13 T. The magnetization and heat capacity could be found in the supplementary Figure S2.

Magnetic torque

The magnetic torque measurements were carried out using piezo-resistive sensor made by Quantum Design, external bridge excitation and Lock-in amplifier readout were utilized. An oriented NCTO single crystal was mounted onto the sensor. The magnetic field was applied in the ab plane, as illustrated in Supplementary Figure S3. Both angular and magnetic field dependent torque measurements were carried out. The low temperature and magnetic field environment were provided by either a Quantum Design PPMS-9 or a top-loading 18T-320mK system.

Inelastic neutron scattering

INS experiments were performed using the SEQUOIA time-of-flight spectrometer at the Spallation Neutron Source, Oak Ridge National Laboratory, USA.[47,48] About 0.559 g samples were fixed on an aluminum sheet with 3 × 6 × 0.05 cm^3 in size, and co-aligned in the (HHL) scattering plane with **B** // **a*** (Supplementary Figure S8). The sample was inserted in a liquid-helium cryostat, reaching a base temperature of T = 2 K. Measurements at 2 K with applied magnetic fields B = 0 T and 8 T were performed by rotating the sample in steps of 1° with E_i = 18 meV and choppers in high-resolution mode, yielding a full-width at half-maximum (FWHM) elastic energy resolution of about 0.41 meV. When the magnet was removed, we collected again the INS data at 0 T and 4.9 K, which also were performed by rotating the sample in steps of 1° with E_i = 18 meV and choppers in high-resolution mode. In order to subtract the background, the INS data were collected at 90 K with or without magnet.

Variational Monte Carlo simulation

The VMC method is a variational approach using Gutzwiller projected mean field states as trial wave functions of spin models. The mean field state is obtained in the slave particle representation, where the spin operators are represented in bilinear form of fermions under a particle number constraint. The mean field parameters are not obtained self-consistently, but are treated as variational parameters whose optimal values are determined by minimizing the trial energy. The trial energy and physical quantities (including the correlation functions) of the Gutzwiller projected state are obtained using Monte Carlo simulations.

RESULTS

Magnetic torque

The magnetic torque of a sample $\boldsymbol{\tau} = \mu_0 V \mathbf{M}\times\mathbf{B}$ is highly sensitive to the external magnetic field **B** when the induced magnetization **M** is not aligned with **B**, where μ_0 denotes the permeability of the vacuum and V the volume of

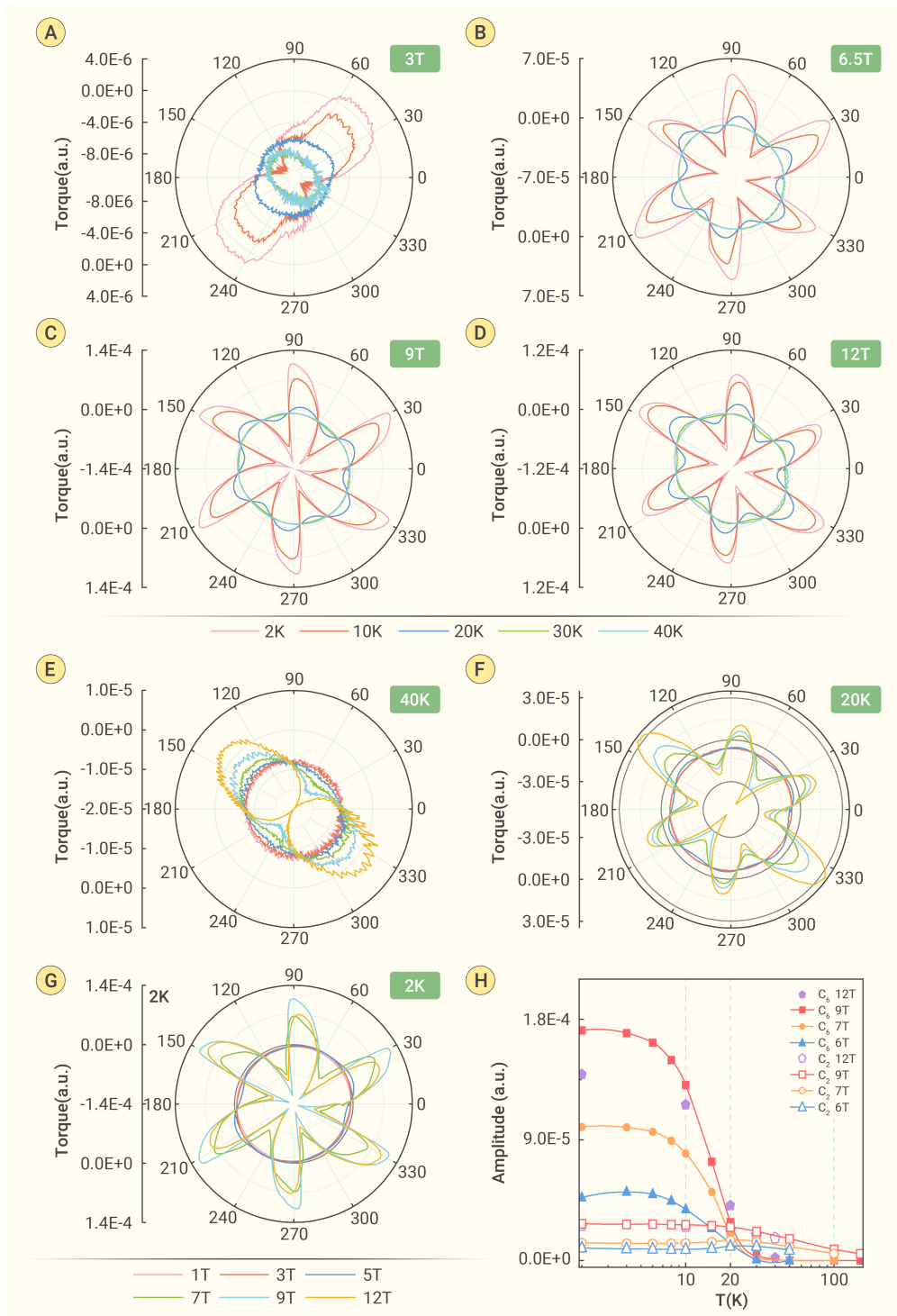

Figure 2. Symmetry evolution of magnetic torque with temperature and magnetic field (A)-(D) Polar plots of magnetic torque $\tau(\theta)$ at different temperatures with the fixed magnetic fields. (E)-(G) Polar plots of magnetic torque $\tau(\theta)$ at different magnetic fields with the fixed temperatures. (H) Temperature-dependent amplitude of C6 and C2 symmetry obtained by Fourier transform of angle-dependent magnetic torque at different fields.

the sample. Therefore, the torque in a uniform **B** is a direct detection of the magnetic anisotropy.

Figures 1F-G show the field dependence of the torque ratio and the first order derivative for field deviating from **a*** counterclockwise in the *ab* plane by angles θ = 2.4°, 5.9°, 10.6°, 14.2°, respectively. Since $\frac{1}{B}\frac{d\tau}{dB} = \mu_0 V\frac{\partial \mathbf{M}}{\partial B}\times\mathbf{n} + \mu_0 V\frac{\mathbf{M}}{B}\times\mathbf{n}$, with $\mathbf{B} = B\mathbf{n}$ where **n** is the unit vector along the field direction, the quantity $\frac{1}{B}\frac{d\tau}{dB}$ contains the information of the off-diagonal differential magnetic susceptibility and is thus helpful for locating the phase boundaries (Figure 1G).

At low temperatures, three phase transitions can be identified by the anomalies in the field derivative ($\frac{1}{B}\frac{d\tau}{dB}$) where B_{C1} is the transition field from the zigzag- phase to an intermediate region labeled as '*X*', B_{C2} is the critical field from the *X*-region to a magnetically disordered phase, and the B_{C3} is the threshold of the trivial polarized phase.[1] The values of the critical field strength B_{C1}, B_{C2} and B_{C3} slightly vary with the angle θ, but the features of the three transitions are qualitatively unchanged. The anomalies of the $\frac{1}{B}\frac{d\tau}{dB}$ curves become weak when θ approaches 0° (but the three critical fields are still consistent with the differential susceptibility dM/dB curve at θ = 0° in Figure 1G). Therefore, for clarity we choose the critical fields at θ = 10.6° to construct the temperature-field phase diagram (Figure 1C). The critical fields obtained from specific heat measurements with **B** // **a*** (Figure S2E), are comparable with the ones obtained by the torque measurements at θ = 10.6°. Notice that the field-dependent magnetic torque and magnetization both show obvious hysteresis near B_{C1} (Figure S5), indicating the transition is first-order. This is further verified by the clear hysteresis loop in the angular dependence of the torque around 6 T (Figure S4).

The angular dependence of the torque $\tau(\theta)$ directly reflects the symmetry of the magnetic status.[49-51] Since **a*** is the easy axis, the induced magnetization **M** is parallel to **a*** if **B** // **a*** (i.e. for θ = n × 60°, n is an integer), see Figures 2B-D. As the space group of NCTO is $P6_322$ (No.182) whose point group is D_6, $\tau(\theta)$ should exhibit a C_6 symmetry (namely $2\pi/6$ periodicity) if there is no symmetry breaking. As shown in Figure 2A, $\tau(\theta)$ only shows a C_2 symmetry for B = 3 T. This indicates a rotation symmetry breaking in NCTO (from C_6 to C_2) which confirms the AFM long-range order in weak magnetic fields below T_N. Since the thermal fluctuations tend to melt the symmetry breaking orders, the symmetry of $\tau(\theta)$ is expected to increase with increasing temperature and eventually reaches the C_6 in the paramagnetic state above T_N. However, as shown in Figures 2E & H, above T_N, the symmetry is still C_2 with a different orientation. A possible reason for these inconsistences is that the magnetic field is not perfectly lying in the *ab*-plane (the *c*-direction is not strictly parallel to the rotation axis, Figure S3), thus the absolute value of the angle between the field and the *c*-axis oscillates with a 2-fold periodicity.[52] Since the effective in-plane and out-of-plane *g*-factors are different, g_{ab} = 4.13 and g_c = 2.3,[1] the oscillation of the field component along the *c*-direction results in the two-fold periodic pattern in $\tau(\theta)$.

Meanwhile, strong magnetic field and quantum spin fluctuations can also suppress the zigzag order and restore the symmetry. As shown in Figures 2B-D & G, in the angle-dependent torque data the 6-fold symmetry indeed shows up above B_{C1} = 6 T at low temperatures with coexisting C_2 symmetry. The C_6 symmetry becomes almost perfect when the AFM order is completely suppressed at B_{C2} = 7.5 T. Above B_{C3} = 10 T, the magnitude of the torque

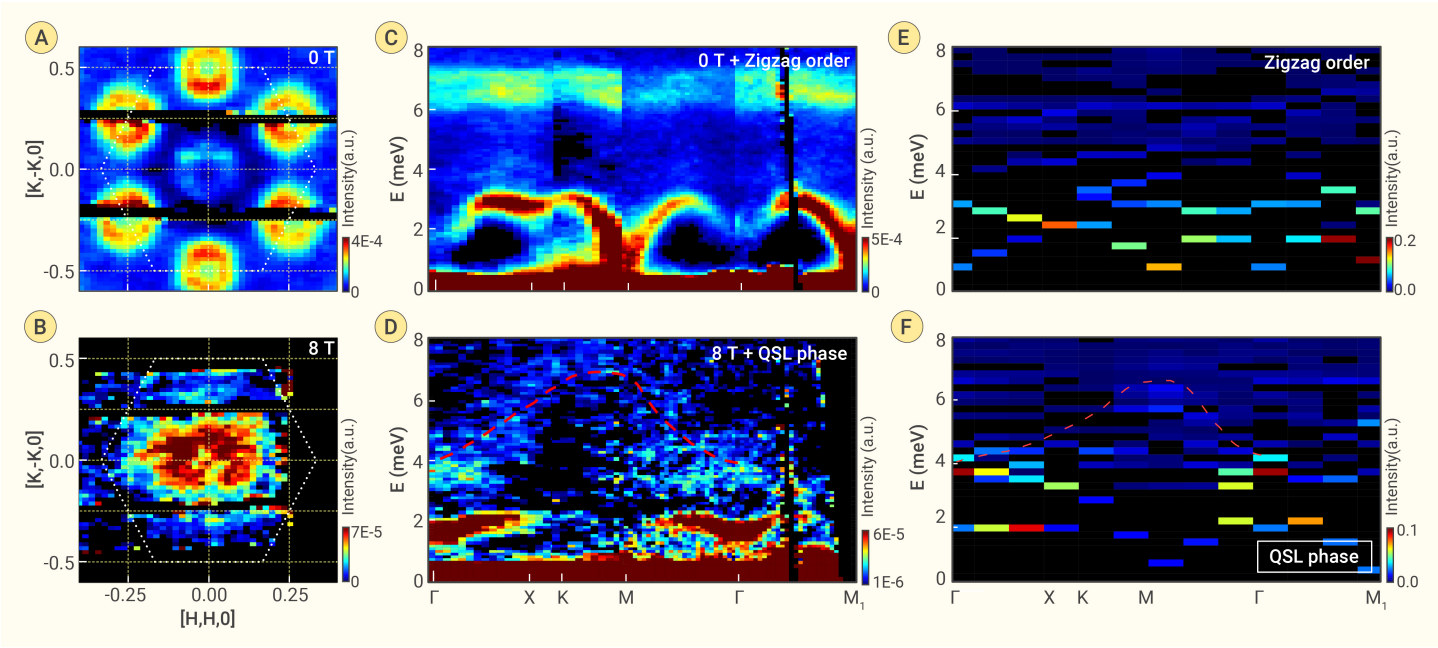

Figure 3. (Color online) Spin-excitation spectra using fixed incident energy E_i = 18 meV with B // a* Constant-energy scattering at 0 T (A) and 8 T (B), respectively, integrated over L = [-2.5, 2.5] and E = [1.5, 2.5] meV, projected on the reciprocal honeycomb plane defined by the perpendicular directions [H, H,0] and [K, -K, 0]. The white dashed lines represent the Brillouin zone boundaries. (C) and (D) Spin-excitation spectra along high symmetry momentum directions Γ-X-K-M-Γ-M_1 at 5 K for zero field and 2 K for 8 T, respectively. The color bar indicates scattering intensity with arbitrary unit in linear scale. The dark red dashed line indicates that an intense 'Λ' shape spinon continuum appears at 4 meV ~ 8 meV in Figure (D). (E) and (F) Calculated dynamic structure factor for the zigzag AFM order and field-induced QSL with partially polarized spins, respectively. The black regions lack detector coverage. The dark red dashed line shows the same 'Λ' shape spinon continuum, which is compared to the experiment at 8T. The data were collected using the SEQUOIA chopper spectrometer at the Spallation Neutron Source (SNS).

decreases with field strength for a polarized phase with diminished quantum fluctuations. The most interesting physics falls in the region between B_{C2} and B_{C3}, a field-induced disordered state with fairly strong quantum fluctuations which is likely to be a QSL phase. Later we will provide theoretical and further experimental evidences to verify the QSL phase. The region *X* between B_{C1} and B_{C2} is considered as a phase with coexisting AFM and topological order (Figure S6). It should be mentioned that the $\tau(\theta)$ pattern of the QSL region (above B_{C2}) still does not show a strict C_6 symmetry with some mild amplitude modulation of 2π/2 period (Figures 2C & F). Those 2-period Fourier components are the same as that of the high-temperature paramagnetic state (Figure S6), hence, this should also be the issue of field alignment mentioned above.

This field-induced intermediate QSL phase is supported by the Variational Monte Carlo (VMC) simulation with a K-J_1-Γ-Γ'-J_3 model (J_1 is the first-neighbor Heisenberg exchange, the values of the parameters will be discussed later), where four phases are obtained with **B** // **a***-axis including the zigzag phase, an intermediated phase with coexisting magnetic order and topological order, the filed-induced QSL phase and the polarized trivial phase (Figure S10). Especially, fixing the field's strength and varying the field's direction in the QSL phase, the induced magnetization **M** is parallel to **B** as **B** is along the **a***- or **a**-direction. When the field is deviated from **a** or **a***, **M** contains nonzero component in a direction perpendicular to the field, which gives rise to nonzero magnetic torque. As shown in Supplementary Figure S12, the simulated magnetization indeed exhibits a 6-fold periodicity in the QSL region, which is consistent with the experimental data shown in Figures 2C & G.

Neutron scattering

To further verify the field induced QSL behavior, we performed scattering measurements at 2 K in the (HHL) plane with **B** // **a***-direction ([K, -K, 0]) at 0 T and 8 T. As shown in Figure 1D, at zero field, the magnetic Bragg reflections can be observed at the M-point (such as [-1/2, 0, 0] and [0, -1/2, 0]), which presents the zigzag AFM order. At 8 T, these magnetic Bragg reflections at the M-points completely disappear but a new Bragg reflection appears at the Γ-point for the partial polarization (Figure 1E).

More interestingly, the applied field also dramatically changes the spin excitation spectrum. Figure 3A presents the momentum dependence of INS intensity integrated from 1.5 to 2.5 meV at 4.9 K and 0 T. The ring-shaped spectra are clearly seen around the M-points, which can be identified as magnon excitations in the zigzag ordered ground state. At the Γ-point, some excitations also show up with smaller weight compared to the M-point. Figure 3B shows the INS intensity integrated from 1.5 to 2.5 meV at T = 2 K and |**B**| = 8 T, where the intensity is concentrated at the Γ-point and represents the edge of a magnon band.

To further reveal the intrinsic spin dynamics of the magnetic Co^{2+} ions, we plot the energy-momentum spectrum of the spin excitations along several high-symmetry points in the first Brillouin zone (Figure 1D). At zero field, a gapped magnon band is shown in Figure 3C, where the minimum point of the band has the largest intensity weight and locates at the M-point as expected. Furthermore, almost flat magnon bands appear at 6 ~ 7 meV. To understand the experimental observations, we theoretically study the zero-field dynamic structure factors in the zigzag ground state and the VMC numerical results are shown in Figure 3E. The shape of the lowest energy spin-wave band agrees well with the experimental data (Figure 3C). The band from VMC at 6 meV is almost flat, and the intermediate weights between the lowest band (< 3 meV) and the flat band (> 6 meV) show up. These features are consistent with experiment in Figure 3C.[34]

With increasing field, the largest intensity of magnetic excitations shifts from the M-point to the Γ-point. At 8 T, around the Γ-point, a band of concave shape shows up at 1.5 meV ~ 2.5 meV and another band of convex shape appears at 3 ~ 4 meV. These two bands, which look like the upper lip and the lower lip, are constituted by single-particle-like magnon excitations. Away from the Γ-point, the weights of the two magnon bands decay rapidly. Instead, a large piece of continuum is observed at higher energy, indicating the existence of fractional excitations beyond the linear-spin-wave theory which predicts only two magnon bands. The continuum extends to the whole Brillouin zone, and its lower edge is overlapping with the upper-lip shaped magnon band. Along the Γ-X-K-M-Γ path, the bright weights of the continuum in the energy range 4 ~ 8 meV form a 'Λ' shape. The pattern of momentum-energy distribution and the fairly strong intensity rule out the possibility of two-magnon continuum. Thus, the continuum is most likely formed by two-spinon fractionalized excitations. The coexistence of (incomplete) single-

particle-like magnon bands and fractionalized continuum is the most exciting observation of the present work. From the strong continuum excitations and the C_6 symmetry of the torque, we infer that NCTO enters a field-induced QSL phase with partial spin polarization and strong quantum fluctuations at 8 T and low temperature.

The dynamical structure factor of the field-induced QSL phase obtained from VMC simulation (Figure 3F), captures most of the important features of the neutron experiment. (1) Both single-particle-like magnon bands and the spinon-continuum are obtained. The magnon modes are dispersive in-gap two-spinon bound states, which form two bands. Above the magnon bands a continuum is formed by fractionalized spinons. The energy ranges of the magnon band and the continuum agree with experiment. (2) In the vicinity of the Γ-point, the two magnon bands form the shape of a lower lip and an upper lip. Similar lip-structure also exists in the linear spin-wave dispersion and is resulting from the significant J_3 interactions. Nonzero magnon weights appear at the M- and M_1-points with energies close to zero. These features agree with the experiment. (3) The lower edge of the continuum is overlapping with the upper magnon band. From 4 meV to 8 meV, the bright weights of the continuum form a shape of 'Λ', which qualitatively agrees with the experiment. (4) The phase has 4-fold topological degenerate ground states on a torus as the emergence of deconfined Z_2 gauge fluctuations and the Z_2 QSL nature of the low energy physics. The deconfined Z_2 gauge charges, namely, the Majorana-fermion like spinons, give rise to the continuum spectrum in the dynamical structure and interpret the experimental weights at 4 ~ 8 meV. Especially, in the intermediate field region the linear spin wave spectrum based on a fully polarized state contains imaginary part around the M-points (Figure S14C), hence, this phase is distinct from the fully polarized phase and is beyond the description of linear-spin-wave theory. To verify the validity of the VMC computations, we performed analytic calculations using random phase approximations (RPA), Figures S15-S16, and the RPA results qualitatively agree with those of the VMC.

DISCUSSION AND CONCLUSION

In our theoretical simulation, we adopted the parameters J_1 = −1.54 meV, J_3 = 1.32 meV, K = 1.408 meV, Γ = −1.32 meV, and Γ' = 0.88 meV, which are equivalent to J_1 = 0.066 meV, J_3 = 1.32 meV, K = −3.399 meV, Γ = 0.286 meV, and Γ' = 0.077 meV via the dual transformation. This set of parameters is adopted from the tx+ model,[46] but with enlarged J_3 and globally multiplied by a constant. The importance of J_3 has been implied in previous works.[1,29,34,35,38-40,46,53] In the 3*d* Co-based honeycomb geometry, the hopping integral associated with the 90° e_g-ligand hybridization plays a significant role through the large σ-type hopping process t^{σ}_{pd}, which is particularly relevant for the third neighbor J_3 super-exchanges in honeycomb materials.[24,38] Moreover, the ratio Δ/λ between the trigonal crystal field (Δ) and the SOC (λ) can regulate the spin-orbit entanglement.[24] With the increasing of Δ/λ, the orbital degeneracy is lifted and the spin-orbit entanglement is suppressed. Powder INS analysis of λ = 21 meV and Δ = 13 meV with a small ratio Δ/λ ~ 0.62 indicates that the spin and orbit are highly entangled.[35]

In summary, based on the magnetic torque and neutron scattering experiments, we studied the magnetic phase diagram and the nature of each phase of NCTO under in-plane magnetic fields, especially **B** // **a***. At low temperatures, NCTO belongs to the zigzag AFM phase under field below B_{C1} = 6 T and enters the trivial polarized phase above B_{C3} = 10 T. As the field is between B_{C2} = 7.5 T and B_{C3} = 10 T, the restoration of the 6-fold symmetry in the angular dependence of the torque strongly indicates that NCTO falls in a field-induced disordered state with strong quantum spin fluctuations. Furthermore, the strong continuum in the INS spectrum and the magnon-like excitations near the Γ-point confirm that this disordered state is a QSL state and the spins are partially polarized. Our theoretically obtained spin excitation spectra from VMC simulations of the effective K-J_1-Γ-Γ'-J_3 model, including the dynamical structure factors of the AFM phase and the partially polarized QSL phase, agree with the experimental data, and support the field-induced QSL behavior in NCTO. Finally, we identify the intermediate X-region between B_{C1} = 6 T and B_{C2} = 7.5 T as a phase with coexisting AFM order and Z_2 topological order.

REFERENCES

1. Lin, G., Jeong, J., Kim, C., et al. (2021). Field-induced quantum spin disordered state in spin-1/2 honeycomb magnet $Na_2Co_2TeO_6$. Nat. Commun. **12**: 5559. DOI: 10.1038/s41467-021-25567-7.
2. Broholm, C., Cava, R.J., Kivelson, S.A., et al. (2020). Quantum spin liquids. Science **367**: 263. DOI: 10.1126/science.aay0668.
3. Shen, Y., Li, Y.-D., Wo, H., et al. (2016). Evidence for a spinon Fermi surface in a triangular-lattice quantum-spin-liquid candidate. Nature **540**: 559–562. DOI: 10.1038/nature20614.
4. Fu, M., Imai, T., Han, T.-H., et al. (2015). Evidence for a gapped spin-liquid ground state in a kagome Heisenberg antiferromagnet. Science **350**: 655–658. DOI: 10.1126/science.aab2120.
5. Okamoto, Y., Nohara, M., Aruga-Katori, H., et al. (2007). Spin-liquid state in the S = 1/2 hyperkagome antiferromagnet $Na_4Ir_3O_8$. Phys. Rev. Lett. **99**: 137207. DOI: 10.1103/PhysRevLett.99.137207.
6. Li, Y.-D., Wang, X., and Chen, G. (2016). Anisotropic spin model of strong spin-orbit-coupled triangular antiferromagnets. Phys. Rev. B **94**: 035107. DOI: 10.1103/PhysRevB.94.035107.
7. Lin, G. and Ma, J. (2023). Is there a pure quantum spin liquid. The Innovation **4**: 100484. DOI: 10.1016/j.xinn.2023.100484.
8. Kitaev, A. (2006). Anyons in an exactly solved model and beyond. Ann. Phys. **321**: 2–111. DOI: 10.1016/j.aop.2005.10.005.
9. Yokoi, T., Ma, S., Kasahara, S., et al. (2021). Half-integer quantized anomalous thermal Hall effect in the Kitaev material candidate a-$RuCl_3$. Science **373**: 568–572. DOI: 10.1126/science.aay5551.
10. Tanaka, O., Mizukami, Y., Harasawa, R., et al. (2022). Thermodynamic evidence for a field-angle-dependent Majorana gap in a Kitaev spin liquid. Nat. Phys. **18**: 429–435. DOI: 10.1038/s41567-021-01488-6.
11. Sears, J.A., Chern, L.E., Kim, S., et al. (2020). Ferromagnetic Kitaev interaction and the origin of large magnetic anisotropy in α-$RuCl_3$. Nat. Phys. **16**: 837–840. DOI: 10.1038/s41567-020-0874-0.
12. Kasahara, Y., Ohnishi, T., Mizukami, Y., et al. (2018). Majorana quantization and half-integer thermal quantum Hall effect in a Kitaev spin liquid. Nature **559**: 227–231. DOI: 10.1038/s41586-018-0274-0.
13. Janša, N., Zorko, A., Gomilšek, M., et al. (2018). Observation of two types of fractional excitation in the Kitaev honeycomb magnet. Nat. Phys. **14**: 786–790. DOI: 10.1038/s41567-018-0129-5.
14. Do, S.-H., Park, S.-Y., Yoshitake, J., et al. (2017). Majorana fermions in the Kitaev quantum spin system α-$RuCl_3$. Nat. Phys. **13**: 1079–1084. DOI: 10.1038/nphys4264.
15. Banerjee, A., Yan, J., Knolle, J., et al. (2017). Neutron scattering in the proximate quantum spin liquid a-$RuCl_3$. Science **356**: 1055–1059. DOI: 10.1126/science.aah6015.
16. Maksimov, P.A. and Chernyshev, A.L. (2020). Rethinking α-RuC_{l3}. Phys. Rev. Res. **2**: 033011. DOI: 10.1103/PhysRevResearch.2.033011.
17. Laurell, P. and Okamoto, S. (2020). Dynamical and thermal magnetic properties of the Kitaev spin liquid candidate α-$RuCl_3$. npj Quantum Mater. **5**: 1–10. DOI: 10.1038/s41535-019-0203-y.
18. Wang, J., Normand, B., and Liu, Z.-X. (2019). One proximate Kitaev spin liquid in the K-J-Γ model on the honeycomb lattice. Phys. Rev. Lett. **123**: 197201. DOI: 10.1103/PhysRevLett.123.197201.
19. Chaloupka, J., Jackeli, G., and Khaliullin, G. (2010). Kitaev-heisenberg model on a honeycomb lattice: Possible exotic phases in Iridium oxides A_2IrO_3. Phys. Rev. Lett. **105**: 027204. DOI: 10.1103/PhysRevLett.105.027204.
20. Banerjee, A., Bridges, C.A., Yan, J.Q., et al. (2016). Proximate Kitaev quantum spin liquid behaviour in a honeycomb magnet. Nat. Mater. **15**: 733–740. DOI: 10.1038/nmat4604.
21. Chaloupka, J., Jackeli, G., and Khaliullin, G. (2013). Zigzag magnetic order in the Iridium oxide Na_2IrO_3. Phys. Rev. Lett. **110**: 097204. DOI: 10.1103/PhysRevLett.110.097204.
22. Jackeli, G. and Khaliullin, G. (2009). Mott insulators in the strong spin-orbit coupling limit: From heisenberg to a quantum compass and Kitaev models. Phys. Rev. Lett. **102**: 017205. DOI: 10.1103/PhysRevLett.102.017205.
23. Takagi, H., Takayama, T., Jackeli, G., et al. (2019). Concept and realization of Kitaev quantum spin liquids. Nat. Rev. Phys. **1**: 264–280. DOI: 10.1038/s42254-019-0038-2.
24. Liu, H., Chaloupka, J., and Khaliullin, G. (2020). Kitaev spin liquid in 3d transition metal compounds. Phys. Rev. Lett. **125**: 047201. DOI: 10.1103/PhysRevLett.125.047201.
25. Hermanns, M., Kimchi, I., and Knolle, J. (2018). Physics of the Kitaev model: Fractionalization, dynamic correlations, and material connections. Ann. Rev. Conden. Matter Phys. **9**: 17–33. DOI: 10.1146/annurev-conmatphys-033117-053934.
26. Kitagawa, K., Takayama, T., Matsumoto, Y., et al. (2018). A spin-orbital-entangled quantum liquid on a honeycomb lattice. Nature **554**: 341–345. DOI: 10.1038/nature25482.
27. Hwan Chun, S., Kim, J.-W., Kim, J., et al. (2015). Direct evidence for dominant bond-directional interactions in a honeycomb lattice iridate Na_2IrO_3. Nat. Phys. **11**: 462–466. DOI: 10.1038/nphys3322.
28. Zhong, R., Guo, S., Xu, G., et al. (2019). Strong quantum fluctuations in a quantum spin liquid candidate with a Co-based triangular lattice. P. Natl. Acad. Sci. USA **116**: 14505–14510. DOI: 10.1073/pnas.1906483116.

29. Winter, S.M. (2022). Magnetic couplings in edge-sharing high-spin d^7 compounds. J. Phys. Mater. **5**: 045003. DOI: 10.1088/2515-7639/ac94f8.
30. Bruin, J.A.N., Claus, R.R., Matsumoto, Y., et al. (2022). Robustness of the thermal Hall effect close to half-quantization in α-$RuCl_3$. Nat. Phys. **18**: 401–405. DOI: 10.1038/s41567-021-01501-y.
31. Czajka, P., Gao, T., Hirschberger, M., et al. (2021). Oscillations of the thermal conductivity in the spin-liquid state of α-$RuCl_3$. Nat. Phys. **17**: 915–919. DOI: 10.1038/s41567-021-01243-x.
32. Chen, L., Gu, Y., Wang, Y., et al. (2023). Large negative magnetoresistance beyond chiral anomaly in topological insulator candidate $CeCuAs_2$ with spin-glass-like behavior. The Innovation Materials **1**: 100011. DOI: 10.59717/j.xinn-mater.2023.100011.
33. Ma, J. (2023). Spins don't align here. Nat. Phys. **19**: 922. DOI: 10.1038/s41567-023-02041-3.
34. Yao, W., Iida, K., Kamazawa, K., et al.. (2022). Excitations in the ordered and paramagnetic states of honeycomb magnet $Na_2Co_2TeO_6$. Phys. Rev. Lett. **129**: 147202. DOI: 10.1103/PhysRevLett.129.147202.
35. Kim, C., Jeong, J., Lin, G., et al. (2021). Antiferromagnetic Kitaev interaction in J_{eff} = 1/2 cobalt honeycomb materials $Na_3Co_2SbO_6$ and $Na_2Co_2TeO_6$. J. Phys.- Condens. Mat. **34**: 045802. DOI: 10.1088/1361-648X/ac2644.
36. Rau, J.G., Lee, E.K.-H., and Kee, H.-Y. (2014). Generic spin model for the honeycomb Iridates beyond the Kitaev limit. Phys. Rev. Lett. **112**: 077204. DOI: 10.1103/PhysRevLett.112.077204.
37. Winter, S.M., Li, Y., Jeschke, H.O., et al.. (2016). Challenges in design of Kitaev materials: Magnetic interactions from competing energy scales. Phys. Rev. B **93**: 214431. DOI: 10.1103/PhysRevB.93.214431.
38. Liu, H. (2021). Towards Kitaev spin liquid in 3d transition metal compounds. Int. J. Mod. Phys. B **35**: 21300061. DOI: 10.1142/s0217979221300061.
39. Hong, X., Gillig, M., Hentrich, R., et al. (2021). Strongly scattered phonon heat transport of the candidate Kitaev material $Na_2Co_2TeO_6$. Phys. Rev. B **104**: 144426. DOI: 10.1103/PhysRevB.104.144426.
40. Chen, W., Li, X., Hu, Z., et al. (2021). Spin-orbit phase behavior of $Na_2Co_2TeO_6$ at low temperatures. Phys. Rev. B **103**: 180404. DOI: 10.1103/PhysRevB.103.L180404.
41. Songvilay, M., Robert, J., Petit, S., et al. (2020). Kitaev interactions in the Co honeycomb antiferromagnets $Na_3Co_2SbO_6$ and $Na_2Co_2TeO_6$. Phys. Rev. B **102**: 224429. DOI: 10.1103/PhysRevB.102.224429.
42. Bera, A.K., Yusuf, S.M., Kumar, A., et al.. (2017). Zigzag antiferromagnetic ground state with anisotropic correlation lengths in the quasi-two-dimensional honeycomb lattice compound $Na_2Co_2TeO_6$. Phys. Rev. B **95**: 094424. DOI: 10.1103/PhysRevB.95.094424.
43. Lefrançois, E., Songvilay, M., Robert, J., et al. (2016). Magnetic properties of the honeycomb oxide $Na_2Co_2TeO_6$. Phys. Rev. B **94**: 214416. DOI: 10.1103/PhysRevB.94.214416.
44. Pilch, P., Peedu, L., Bera, A.K., et al. (2023). Field- and polarization-dependent quantum spin dynamics in the honeycomb magnet $Na_2Co_2TeO_6$: Magnetic excitations and continuum. Phys. Rev. B **108**: 140406. DOI: 10.1103/PhysRevB.108.L140406.
45. Samarakoon, A.M., Chen, Q., Zhou, H., et al.. (2021). Static and dynamic magnetic properties of honeycomb lattice antiferromagnets $Na_2M_2TeO_6$, M = Co and Ni. Phys. Rev. B **104**: 184415. DOI: 10.1103/PhysRevB.104.184415.
46. Sanders, A.L., Mole, R.A., Liu, J., et al. (2022). Dominant Kitaev interactions in the honeycomb materials $Na_3Co_2SbO_6$ and $Na_2Co_2TeO_6$. Phys. Rev. B **106**: 014413. DOI: 10.1103/PhysRevB.106.014413.
47. Stone, M.B., Niedziela, J.L., Abernathy, D.L., et al. (2014). A comparison of four direct geometry time-of-flight spectrometers at the Spallation Neutron Source. Rev. Sci. Instrum. **85**: 045113. DOI: 10.1063/1.4870050.
48. Granroth, G.E., Kolesnikov, A.I., Sherline, T.E., et al. (2010). SEQUOIA: A newly operating chopper spectrometer at the SNS. J. Phys.: Conf. Ser. **251**: 012058. DOI: 10.1088/1742-6596/251/1/012058.
49. Isono, T., Kamo, H., Ueda, A., et al. (2014). Gapless quantum spin liquid in an organic Spin-1/2 triangular-lattice κ-H_3(Cat-EDT-TTF)$_2$. Phys. Rev. Lett. **112**: 177201. DOI: 10.1103/PhysRevLett.112.177201.
50. Okazaki, R., Shibauchi, T., Shi, J., et al. (2011). Rotational symmetry breaking in the hidden-order phase of URu_2Si_2. Science **331**: 439–442. DOI: 10.1126/science.1197358. DOI: 10.1126/science.1197358.
51. Leahy, I.A., Pocs, C.A., Siegfried, P.E., et al. (2017). Anomalous thermal conductivity and magnetic torque response in the honeycomb magnet α-$RuCl_3$. Phys. Rev. Lett. **118**: 187203. DOI: 10.1103/PhysRevLett.118.187203.
52. Asaba, T., Lawson, B.J., Tinsman, C., et al. (2017). Rotational symmetry breaking in a trigonal superconductor Nb-doped Bi_2Se_3. Phys. Rev. X **7**: 011009. DOI: 10.1103/PhysRevX.7.011009.
53. Lee, C.H., Lee, S., Choi, Y.S., et al. (2021). Multistage development of anisotropic magnetic correlations in the Co-based honeycomb lattice $Na_2Co_2TeO_6$. Phys. Rev. B **103**: 214447. DOI: 10.1103/PhysRevB.103.214447.

ACKNOWLEDGMENTS

We gratefully acknowledge the helpful discussions of Dr. Tian Shang, East China Normal University. J.M. and Z.X.L. thank the financial support from the National Key Research and Development Program of China (Grant Nos. 2022YFA1402702, 2018YFA0704300, and 2023YFA1406500). G.T.L, Z.X.L., and J.M. thank the National Science Foundation of China (Nos. U2032213, 11774223, 12004243, 11974421, 12374166 and 12134020). J.M. thanks the interdisciplinary program Wuhan National High Magnetic Field Center (Grant No. WHMFC 202122), Huazhong University of Science and Technology, and a Shanghai talent program. G.T.L thanks the projects funded by China Postdoctoral Science Foundation (Grant No. 2022T150414) and the Startup Fund for Young Faculty at SJTU (24X010500168). Q.H. and H.D.Z. thank the support from NSF-DMR-2003117. M.F.S thanks the support from Guangdong Provincial Key Laboratory of Extreme Conditions (Grant No. 2023B1212010002). H.W.C. thanks the support from the Collaborative Innovation Program of Hefei Science Center, CAS (Grants No. 2021HSC-KPRD003). This research used resources at the Spallation Neutron Source, a DOE Office of Science User Facility operated by the Oak Ridge National Laboratory. The work at Michigan is supported by the Department of Energy under Award No. DE-SC0020184 (magnetic torque analysis).

AUTHOR CONTRIBUTIONS

G.T. Lin, and J. Ma conceived and supervised the study and designed the measurement setup. Q. Huang and H.D. Zhou synthesized the high-quality single-crystal samples. G.T. Lin, M.F. Shu, Y.N.N. Ma, J.L. Jiao, J.M. Sheng, L.S. Wu, L. Li and G. Li performed the magnetization, heat capacity, and torque measurements. A. Kolesnikov, G.T. Lin, and J. Ma performed inelastic neutron scattering experiment. G.T. Lin, X.Q. Wang, J. Ma, H.D. Zhou, and Z.X. Liu analyzed the data. Theoretical interpretations and numerical simulations are carried out by Q.R. Zhao, G.J. Duan, R. Yu and Z.X. Liu. G.T. Lin prepared the manuscript with H.D. Zhou, Z.X. Liu and J. Ma. All authors discussed the data and its interpretation.

DECLARATION OF INTERESTS

The authors declare no competing interests.

DATA AND CODE AVAILABILITY

The data that support the findings of this study are available from the corresponding authors upon request.

SUPPLEMENTAL INFORMATION

It can be found online at https://doi.org/10.59717/j.xinn-mater.2024.100082